Neutron interferometer crystallographic imperfections and gravitationally induced quantum interference measurements

B. Heacock, M. Arif, R. Haun, M. G. Huber, D. A. Pushin, and A. R. Young

Phys. Rev. A **95**, 013840 — Published 25 January 2017

DOI: 10.1103/PhysRevA.95.013840

Neutron interferometer crystallographic imperfections and gravitationally-induced quantum interference measurements

B. Heacock,[1,2,*] M. Arif,[3] R. Haun,[4] M. G. Huber,[3] D. A. Pushin,[5,6] and A. R. Young[1,2]

[1] *Department of Physics, North Carolina State University, Raleigh, NC 27695, USA*
[2] *Triangle Universities Nuclear Laboratory, Durham, North Carolina 27708, USA*
[3] *National Institute of Standards and Technology, Gaithersburg, MD 20899, USA*
[4] *Department of Physics, Tulane University, New Orleans, LA 70118, USA*
[5] *Institute for Quantum Computing, University of Waterloo, Waterloo, Ontario N2L 3G1, Canada*
[6] *Department of Physics and Astronomy, University of Waterloo, Waterloo, Ontario N2L 3G1, Canada*

(Dated: December 28, 2016)

Dynamical diffraction leads to an interesting, unavoidable set of interference effects for neutron interferometers. This experiment studies the interference signal from two and three successive Bragg diffractions in the Laue geometry. We find that intrinsic Bragg-plane misalignment in monolithic, "perfect" silicon neutron interferometers is relevant between successive diffracting crystals, as well as within the Borrmann fan for typical interferometer geometries. We show that the dynamical phase correction employed in the Colella, Overhauser and Werner (COW) gravitationally-induced quantum interference experiments is attenuated by slight, intrinsic misalignments between diffracting crystals, potentially explaining the long-standing 1% discrepancy between theory and experiment. This systematic may also impact precision measurements of the silicon structure factor, affecting previous and future measurements of the Debye-Waller factor and neutron-electron scattering length as well as potential fifth-force searches. For the interferometers used in this experiment, Bragg planes of different diffracting crystals were found to be misaligned by 10 nrad to 40 nrad.

I. INTRODUCTION

For the past forty years, single crystal neutron interferometers have demonstrated their robustness in the fields of fundamental physics, quantum mechanics, neutron scattering, nuclear theory, and quantum information. This is due to the neutron's interaction with magnetic and nuclear structure and Earth's terrestrial gravitational field having roughly equal magnitudes and through the high sensitivity gained over other techniques in measuring interference effects. For most interferometry experiments only properties of the sample or interaction being probed are of interest and the details of the physical interferometer can be ignored. However, some of the most interesting neutron interferometry experiments are sensitive to neutron's path and phase accumulated within the crystal beam splitters. Dynamical diffraction, which describes Bragg diffraction within a crystal lattice, describes the inner workings of the interferometer and is dependent on multiple Bragg diffractions constructively interfering before leaving the device.

The standard neutron interferometer consists of several crystals or "blades" for consecutive Bragg diffraction. Bragg scattering requires that each of these blades be aligned relative to each other within the angular acceptance of the silicon crystal, called the Darwin width Θ_{Darwin}; typically between 5 μrad and 25 μrad. For this reason, neutron interferometers are made from a single, float-zone silicon ingot. The blades create a Mach-Zehnder neutron interferometer with several centimeters of path separation. The blades are formed by removing material from the ingot but preserving approximately half the ingot to serve as a common base (see Fig. 1). This common base insures that the crystal blades are aligned relative to each other to within Θ_{Darwin}. Further details of constructing an interferometer can be found in Ref. [11]. Typically, this relative alignment between the blades is assumed to be perfect, even over the relatively large dimensions of the crystal ($\sim$ 10 cm). This assumption, however, is only justified at the microradian level while outside this alignment the interferometer would cease to function. Our work considers how the relative imperfect alignment of these blades at levels over one hundred times smaller than Θ_{Darwin} impacts the performance of the interferometer due to interference effects arising from dynamical Bragg diffraction.

Inside the crystal blades neutrons undergo Bragg diffraction (Fig. 2) where the incoming free particle state splits into two degenerate branches. This is because the solution of the Schrodinger equation within the crystal lattice has two unique solutions per incident momentum mode, $|\boldsymbol{k}\rangle$. Each of the two branches accrues a different dynamical-induced phase which is a function of the incident neutron momentum mode's deviation from the Bragg condition.

For momenta of the incoming particle extremely close to the exact Bragg condition, this leads to the well-known Pendellösung interference in a single diffracting crystal [1]. The two states become at least partially separated in space and can recombine upon subsequent Bragg diffractions. This leads to an interference peak in the reflected intensity as a function of crystal misalignment at the nanoradian scale [2–5]. These effects are also seen in Mach-Zehnder neutron interferometers. For example, dy-

* Corresponding author: bjheacoc@ncsu.edu

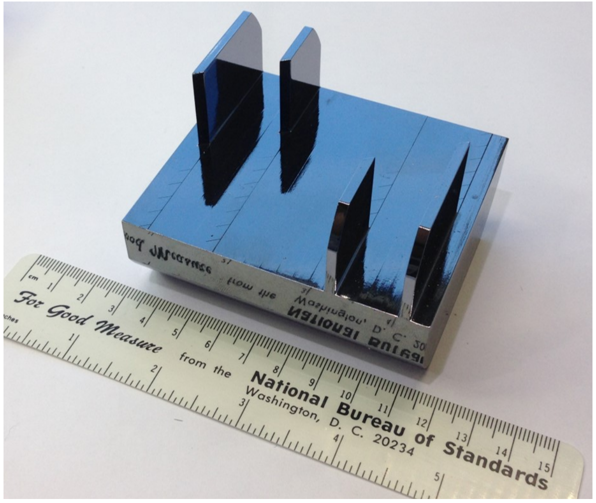

FIG. 1: The crystal interferometer used in the second experiment described in text. Four blades protrude from a common base.

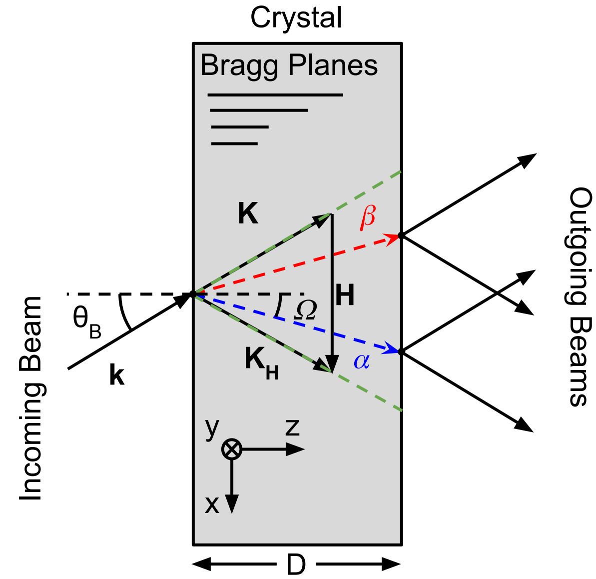

FIG. 2: An incoming momentum state, $|\boldsymbol{k}\rangle$, excites two degenerate, $\{\alpha, \beta\}$, states within the crystal. These two states become spatially separated according to the μrad misalignment of $|\boldsymbol{k}\rangle$ from the exact Bragg condition. Each incoming neutron wavepacket fills the *entire* Borrmann fan (outlined by green-dashed lines).

namical phases affected measurements of gravitationally-induced quantum interference [6–9]. More recently it was demonstrated that one can use a Mach-Zehnder geometry with extra diffracting crystals to measure dynamical phase differences between fully separated beams [10–12].

This work was performed at the National Institute for Standards and Technology (NIST) Center for Neutron Research (NCNR) in Gaithersburg, MD. Following [2–5], two and three crystal rocking curves were measured by counter rotating two fused silica prisms between blades of a neutron interferometer. Our measurements show that both the net offset and variation of intrinsic Bragg plane misalignments are large enough to be relevant between and within diffracting crystal blades. It is then shown that this phenomenon is a possible culprit for the twenty year discrepancy between theory and experiment for measurements of gravitationally-induced quantum interference using a perfect-crystal neutron interferometer [8, 9, 13]. These experiments, beginning in 1975 are commonly referred to as the COW experiments after Colella, Overhauser and Werner, the authors of the first measurement [14]. Bragg plane misalignment will also affect future experiments that measure dynamical phases, such as precision measurements of the silicon structure factor, the measurement of which is sensitive to the Debye-Waller factor, the neutron-electron scattering length, and even fifth forces at the angstrom length scale [15–17].

We begin with the necessary, however unfortunately dense, results from dynamical diffraction theory. Two experiments to measure the net Bragg plane misalignment between diffracting crystals of a neutron interferometer at the nanoradian level are covered in Sec. IV. Finally, we discuss the implications of this systematic on gravitationally-induced quantum interference measurements in Sec. V.

II. DYNAMICAL DIFFRACTION IN PERFECT CRYSTAL NEUTRON INTERFEROMETERS

Dynamical diffraction for the neutron case has been thoroughly treated in the past [18–20]. When a neutron wavepacket undergoes Bragg diffraction in the Laue geometry (the reciprocal lattice vector, $\boldsymbol{H}$, pointed along the crystal surface), the reflected wavepacket has a Lorenzian phase-space profile with a width $\delta k/k \sim v_H/Hk \sim 10^{-6}$, with v_H given by [18]

$$v_H = \frac{4\pi}{a^3} \sum_v b_v e^{i\boldsymbol{H}\cdot\boldsymbol{x}_v}, \tag{1}$$

where the summation is over one unit cell, with a^3 being its volume and b_v the nuclear scattering length of the v^{th} nuclei.

Dynamical phases are incurred from the momentum-space-dependent filling of the Borrmann fan, as shown in Fig. 3. For each incoming neutron momentum mode, two degenerate states are excited within the crystal. These two states, $\{\alpha, \beta\}$, are linear combinations of the transmitted, $|\boldsymbol{k}\rangle$, and diffracted, $|\boldsymbol{k}+\boldsymbol{H}\rangle$, states, and propagate in a direction through the crystal that is a function of the incoming momentum mode's misalignment from Bragg. The definition of these states are given in Appendix A. Neutron momentum modes that are exactly on-Bragg propagate orthogonally to $\boldsymbol{H}$. Off-Bragg components pass through the crystal at an angle [20]

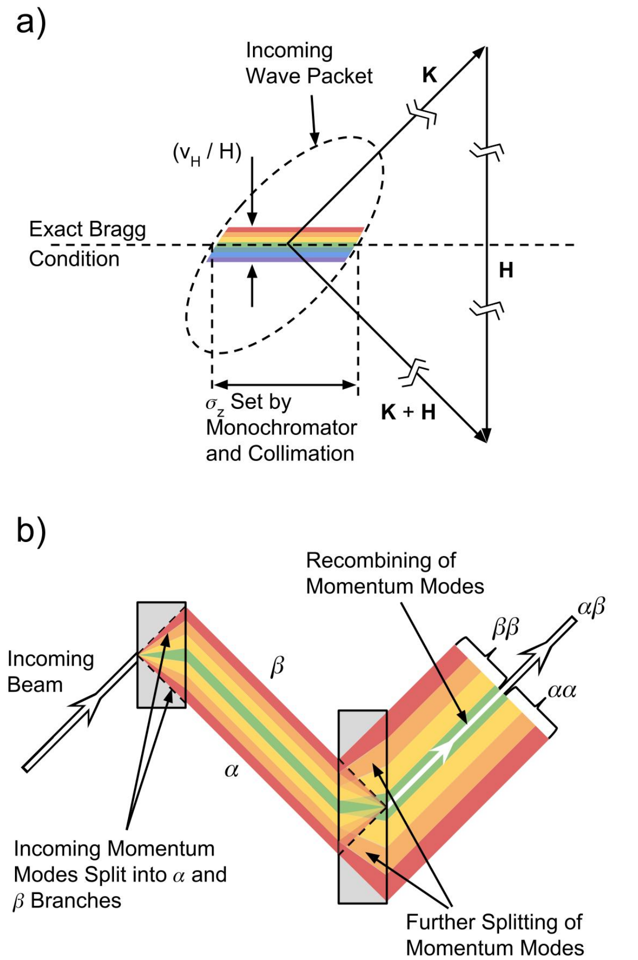

FIG. 3: Dynamical phases in a two crystal geometry. Shown is a momentum-space depiction (a), with the component of $\boldsymbol{k}$ along $\boldsymbol{H}$ selected by the crystal colored. The magnitude of the crystal's angular acceptance relative to the spread of the wavepacket in phase space is greatly exaggerated for clarity. Coherent recombination (b) is dependent on the precise alignment of the crystals and a uniform potential between and within the diffracting crystals. Only the infrared deviations from Bragg are shown; the ultraviolet deviations follow the same pattern.

$$\Omega = \pm\arctan\left\{\frac{\left(K_H^2 - K^2\right)\tan\theta_B}{\sqrt{\left(K_H^2 - K^2\right)^2 + |v_H|^2}}\right\}, \tag{2}$$

where θ_B is the Bragg angle; $\boldsymbol{K}$ is the incident momentum mode inside the crystal; and $\boldsymbol{K}_H = \boldsymbol{K} + \boldsymbol{H}$. Note that $K_H^2 - K^2 = 0$ is another way of writing the Bragg condition, such that $\Omega = 0$ at the exact Bragg condition and $\Omega \to \theta_B$ for increasingly off-Bragg momenta.

In the case of multiple diffracting crystals, the two-fold degenerate splitting of each incoming $|\boldsymbol{k}\rangle$ continues, such that there is a 2^N splitting after N crystals. The α and β states are labeled according to the first crystal, corresponding to the sign of the current density, $J_x^{\alpha,\beta} = \pm\text{sign}\left(H_{x0}\right)|J_x|$, relative to $\boldsymbol{H}$ for the first crystal, $\boldsymbol{H}_0$. If all of the crystals have the same thickness, there are $N+1$ combinations of α and β reflections or transmissions leaving the N^{th} crystal with $N-1$ recombination points (Fig. 4). If the crystals are perfectly aligned and have the same thickness, then there is no phase shift between the permutations of α and β states for each of the $N-1$ recombination points. However, if one crystal is misaligned with respect to another, a momentum-dependent phase shift arises, which quickly leads to dephasing and a loss of contrast in the interferometer. This effect is why perfect crystal neutron interferometers must be cut from single, float-zone grown silicon ingots. Additionally, the interferometer blades are made to have the same thickness to a few micrometers to avoid similar dephasing effects.

III. DYNAMICAL PHASE INTERFERENCE

Dynamical phases affect many diffracting geometries, from single crystal Pendellösung interference [1, 21, 22], to multi-crystal rocking curves [2–5], to traditional Mach-Zehnder neutron interferometers [6, 7, 9], to more complicated geometries [10–12, 16]. Crystal misalignment behaves as a phase shifter for a multi-crystal interference peak [5], implying that such misalignments will change the predicted response of an overall Mach-Zehnder neutron interferometer. To see this, our measurements utilize the geometry depicted in Figs. 4a and 4b. In Fig. 4a we depict how we use a Mach-Zhender inteferometer for our measurements and in Fig. 4b we depict the usual method in which these interferometers are used (for example in the COW experiments). We use the interference peak structure of two and three Bragg reflections to measure Bragg-plane misalignments. We then show how these misalignments affect the phase and contrast of a Mach-Zhender interferometer.

A. Two crystal geometry

It can be shown that the intensity for a twice Bragg reflected neutron is (up to a normalization constant)

$$I = \int \mathrm{d}\Gamma \mathrm{d}k_z \left|\langle\psi|k_z\rangle\right|^2 \sqrt{1-\Gamma^2}\Bigg\{1 - P(D_2) + \frac{1}{2}\cos\left(HD\delta\Gamma\right)\Big[P(D_2 - D_1) - 2P(D_1) + P(D_1 + D_2)\Big]\Bigg\}, \tag{3}$$

where D_1 and D_2 are the thicknesses of the first and second diffracting crystals; δ is the angular Bragg-plane misalignment of the two crystals in the $\boldsymbol{k}, \boldsymbol{H}$ plane; k_z

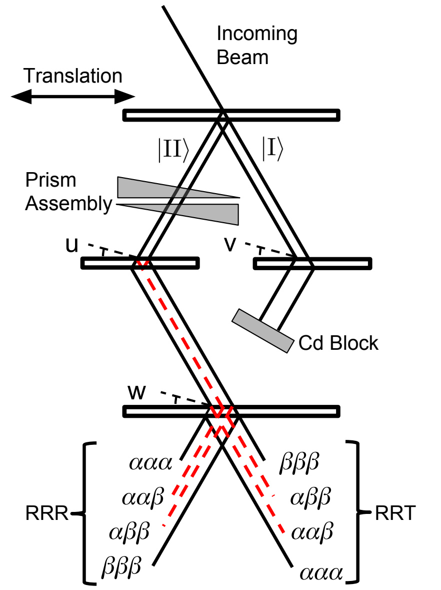

(a) Our experimental setup used to measure intrinsic misalignments in an interferometer.

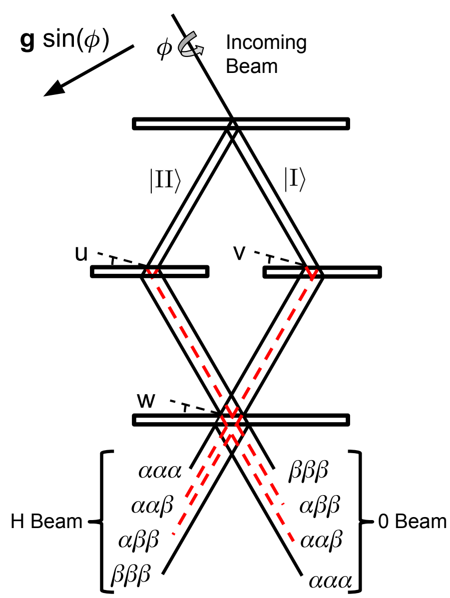

(b) The Mach-Zehnder neutron interferometer geometry used in the COW experiments. Here the direction of gravity is denoted by $\boldsymbol{g}\sin(\phi)$, where ϕ is the interferometer tilt about the incoming beam axis.

FIG. 4

is the neutron momentum along the Bragg planes (see Fig. 2); and $|\langle k_z|\psi\rangle|^2$ is the momentum-space intensity profile of the incoming wavepacket (Fig. 3) along z. The integration variable, Γ, ranges from -1 to 1 and is related to momentum in the $\boldsymbol{H}$ direction [20]

$$\Gamma = \frac{\boldsymbol{k}\cdot\boldsymbol{H}}{\sqrt{(\boldsymbol{k}\cdot\boldsymbol{H})^2 + (H^2/v_H)^2}} \tag{4}$$

$$= \tan(\Omega)/\tan(\theta_B). \tag{5}$$

The function, P, is defined by

$$P(D) = \cos\left(\frac{D|v_H|}{k_z\sqrt{1-\Gamma^2}}\right), \tag{6}$$

which is the origin of Pendellösung interference. Except for $P(D_2 - D_1)$, the $P(D)$ terms correspond to the overlap of states with different combinations of α and β reflections.

For the NIST setup, the width of $|\langle k_z|\psi\rangle|^2$ (Fig: 3) is $\sigma_{kz}/k_z \sim 0.0015\,\mathrm{rad}$, and $|v_H|D/k_z \sim 217$. As a result, the $P(D)$ term is attenuated by only a few percent after the integration of $|\langle\psi|k_z\rangle|^2$ over k_z. However, the range of Γ of $\{-1,1\}$ and the $\sqrt{1-\Gamma^2}$ envelope ensures that the highly oscillatory term

$$P(D) = \cos\left(\frac{|v_H|D}{k_z\sqrt{1-\Gamma^2}}\right) \sim \cos\left(\frac{217}{\sqrt{1-\Gamma^2}}\right) \tag{7}$$

integrates to a small value. In other words, Pendellösung interference terms dephase very quickly for the crystal thicknesses typically used in neutron interferometers of $D \sim 2.5\,\mathrm{mm}$. As a result $P(D)$ terms are often ignored, and most authors use the approximation

$$I \to \int \mathrm{d}\Gamma\sqrt{1-\Gamma^2}\left\{1 + \frac{1}{2}\cos\left(HD\delta\Gamma\right)\right\} = \frac{\pi}{2}\left(1 + \frac{J_1(u)}{u}\right), \tag{8}$$

where J_1 is the first order Bessel function of the first kind, and $u = HD\delta$.

This approximation of letting $P(D) \to 0$ is generally a good one and can be extended to any geometry of diffracting crystals. We therefore will not derive the equivalent of Eqn. 3 for three-crystal rocking curves or Mach-Zehnder interferometers. However, we will explore what we call the "fine structure" in the intensity arising from nonzero $P(D)$ terms in Subsec. IV C for the two crystal rocking curve.

For a more in-depth analysis of a two-crystal interferometer with thick blades the reader is encouraged to see [5]. The authors use a combination of prisms, phase steps, and a slit on the second crystal to characterize the interferometer.

B. Three crystal geometry

In the Pendellösung dephasing limit, $P(D) \to 0$, the interfering portion of a neutron undergoing three Bragg reflections is (Fig. 4) [23]

$$I = \int_{-1}^{1} \mathrm{d}\Gamma (1-\Gamma^2)^{\frac{3}{2}} \Big\{ 3 + 2\cos\left[(u-w)\Gamma\right] + + 2\cos\left[u\Gamma\right] + 2\cos\left[w\Gamma\right] \Big\} = = 6\pi \left(\frac{3}{16} + \frac{J_2(u-w)}{(u-w)^2} + \frac{J_2(u)}{u^2} + \frac{J_2(w)}{w^2} \right), \quad (9)$$

where $u = HD\delta_{1,2}$ and $w = HD\delta_{1,3}$, with $\delta_{i,j}$ the angular misalignment between the i^{th} and j^{th} crystals. The term u in Eqns. 8 and 9 are equivalent. We employ this relationship later to make an absolute measurement of the misalignment

$$HD\delta_{2,3} = u - w. \quad (10)$$

C. Misalignment in a Mach-Zhender Interferometerr

The typical Mach-Zhender geometry is depicted in Fig. 4b, where two spatially separated, coherent beams (I and II) are produced in the first crystal blade and recombined in the final blade, resulting in two interfering beams, the 0 Beam and H Beam. The COW experiments utilize this geometry. We can describe the response of a Mach-Zehnder neutron interferometer to misalignments with three independent variables, $\{u, v, w\}$ (Fig. 4), which describe the misalignment between the two mirror and analyzer crystal blades relative to the initial splitter crystal blade. To do this, we start by writing down the state leaving the interferometer:

$$|\psi\rangle = |\mathrm{I}\rangle + |\mathrm{II}\rangle, \quad (11)$$

where we are coherently adding the states from paths I and II together. Then let

$$|\psi\rangle \to |\mathrm{I}(v,w)\rangle + |\mathrm{II}(u,w)\rangle e^{i\phi_0}, \quad (12)$$

where ϕ_0 is the non-dynamical phase shift between the two paths of the interferometer and $|\mathrm{I}(v,w)\rangle$ and $|\mathrm{II}(u,w)\rangle$ are states that depend on the misalignments $\{u, v, w\}$. Notice that $|\mathrm{I}\rangle$ is not a function u and $|\mathrm{II}\rangle$ is not a function v, so that the misalignment of the mirror crystals for each path need not be the same. Comparing the intensity of the two beams exiting the interferometer to the measured interferogram

$$\langle\psi|\psi\rangle = A + B\cos(\phi_0 + \varphi_D) = \left(\langle\mathrm{I}| + \langle\mathrm{II}|e^{-i\phi_0}\right)\left(|\mathrm{I}\rangle + |\mathrm{II}\rangle e^{i\phi_0}\right). \quad (13)$$

The measured, dynamical phase, φ_D is then [8]

$$\varphi_D = \arctan\left\{ -\frac{\mathrm{Im}\left(\langle\mathrm{I}|\mathrm{II}\rangle\right)}{\mathrm{Re}\left(\langle\mathrm{I}|\mathrm{II}\rangle\right)} \right\}, \quad (14)$$

and the contrast is given by

$$C = \frac{B}{A} = \frac{2\sqrt{\mathrm{Im}\left[\langle\mathrm{I}|\mathrm{II}\rangle\right]^2 + \mathrm{Re}\left[\langle\mathrm{I}|\mathrm{II}\rangle\right]^2}}{\langle\mathrm{I}|\mathrm{I}\rangle + \langle\mathrm{II}|\mathrm{II}\rangle}. \quad (15)$$

In general we can write $|\mathrm{I}, \mathrm{II}\rangle$ in terms of the $\{\alpha, \beta\}$ branches

$$|\mathrm{I},\mathrm{II}\rangle = |\alpha,\alpha,\alpha\rangle_{\mathrm{I,II}} + |\beta,\beta,\beta\rangle_{\mathrm{I,II}} + \Big(|\alpha,\alpha,\beta\rangle_{\mathrm{I,II}} + |\alpha,\beta,\alpha\rangle_{\mathrm{I,II}} + |\beta,\alpha,\alpha\rangle_{\mathrm{I,II}}\Big) + \Big(|\alpha,\beta,\beta\rangle_{\mathrm{I,II}} + |\beta,\alpha,\beta\rangle_{\mathrm{I,II}} + |\beta,\beta,\alpha\rangle_{\mathrm{I,II}}\Big). \quad (16)$$

Different combinations of α and β reflections/transmissions give Pendellösung terms similar to those already discussed in reference to Eqn. 3. Therefore, in the Pendellösung dephasing approximation, the overlap between states with different numbers of α and β reflections/transmissions are taken to be zero when forming $\langle\mathrm{I},\mathrm{II}|\mathrm{I},\mathrm{II}\rangle$. Expressions for $\langle\mathrm{I},\mathrm{II}|\mathrm{I},\mathrm{II}\rangle$ for the 0 Beam are given in Appendix B.

IV. EXPERIMENT

An assembly of two fused silica prisms, each with a pitch of 6°, was placed between the first and second blades of a three-blade interferometer (Fig. 4a). The prism assembly is the same as the one used in [24]. The beam transmitted through the first crystal blade was blocked. The prisms were counter-rotated to deflect the neutron beam in the $\boldsymbol{k}, \boldsymbol{H}$ plane, generating interference peaks in two detectors, labeled RRR and RRT. The $RRR + RRT$ (equivalent to RR) and RRR signals are of interest here and are given by Eqns. 8 and 9, respectively.

Measurements were made with two of the NIST neutron interferometers. For the first interferometer, a single set of RR and RRR curves were measured over a long period of time, so that the uncertainty in the peak position would be low and the fine structure ($P(D) \neq 0$) of the RR curve could be analyzed (see Subsec. IV C). For the second interferometer, the RR and RRR curves were measured as a function of interferometer translation to measure any spatial dependence of the Bragg plane misalignments between crystal blades.

To measure a rocking curve interference peak, the prisms are counter-rotated (Fig. 5) and the beam deflection due the prisms is of the form:

$$\delta_p \propto \tan\gamma \sin\phi \left(\cos\theta + \sin\theta \frac{\tan\gamma\sin\phi + \tan\theta}{1 - \tan\gamma\sin\phi\tan\theta} \right), \quad (17)$$

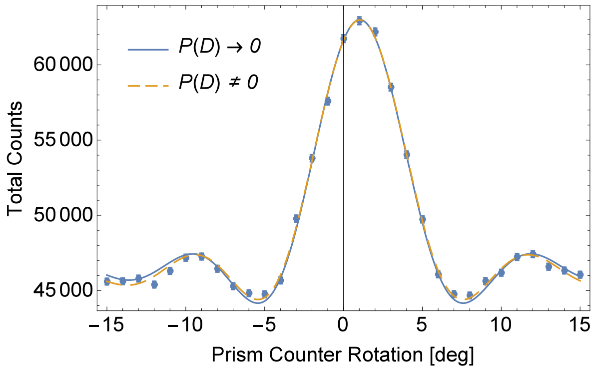

(a) RR Intensity. The $P(D) \to 0$ fit uses Eqn. 20, and the $P(D) \neq 0$ fit is explained in Subsec. IV C.

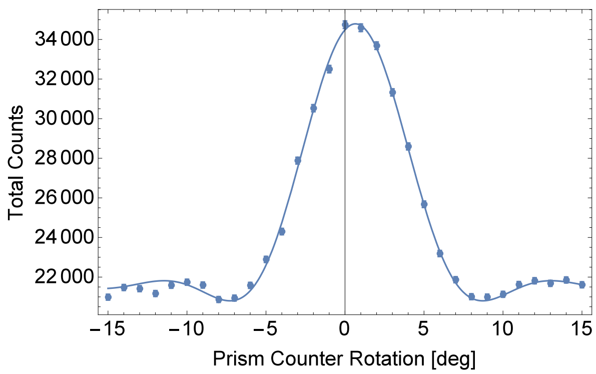

(b) The RRR Intensity with the fit to Eqn. 21.

FIG. 5: RR and RRR summed intensity with fits. Integrated count time was 89 min. per point. Each plot is the sum of 89 individual rocking curves.

where γ is the pitch of the prism; θ is the angle between the prism rotation axis and the neutron beam; and ϕ is the angle of the prism from vertical. For the first set of measurements, the prism assembly was aligned parallel to the interferometer blades, so that $\theta \simeq \theta_B$.

For the second set of measurements, the prism assembly was aligned perpendicular to the beam such that $\theta \simeq 0$. The horizontal spatial dependence of the rocking curve peak positions was measured by translating the interferometer relative to the beam by 1 cm in 1 mm steps, with rocking curves taken for each translational position (Fig. 7). With the translation of the interferometer, the crystal volume probed by neutrons is also shifted. Rocking curve position vs translation thus gives a one dimensional map of the Bragg-plane misalignment between crystal blades as a function of position.

A. Peak Location and Sensitivity

To assess a rocking curve's tendency to drift (similar to the way the phase of a Mach-Zehnder neutron interferometer drifts), the peak position of each RR rocking curve for the first crystal was found by fitting to Eqn. 20, which is defined in the next section; included is an explanation of how the peak locations can be reported in terms of an intrinsic angular alignment. The set of 89 rocking curve positions fit a Gaussian distribution ($\exp[-(x-\mu)^2/(2\sigma^2)]$), with $\mu = (16.9 \pm 0.4)$ nrad and $\sigma = (3.24 \pm 0.34)$ nrad (Fig. 6). The peak locations are stable, and the uncertainty matches that which is predicted by counting statistics; the average peak location uncertainty was 2.94 nrad. Furthermore, averaging the 89 individual rocking curve positions gives (16.78 ± 0.31) nrad, which is indistinguishable from fitting the combined data to Eqn. 20. This yields a peak location of (16.37 ± 0.31) nrad. The average reduced χ^2 (DOF $= 31 - 4$) for the 89 individual rocking curve fits was 1.1. The reduced χ^2 for the combined fit was 2.8.

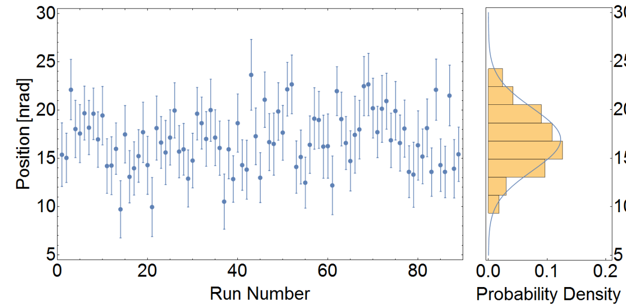

FIG. 6: Fitted peak locations follow the distribution predicted by counting statistics. The average uncertainty in the individual rocking curve peak positions was 2.94 nrad. This is to be compared to fitting the set of 89 rocking curve peak positions to a Gaussian distribution, which gives $\sigma = (3.24 \pm 0.34)$ nrad.

The interference structure outside the central peak is undetectable in an individual rocking curve, yet can be resolved from summing many rocking curves together. Complications arising from Pendellösung interference may explain why the χ^2 from the single rocking curve is inferior to the χ^2 from 89 individual fits (See Subsec. IV C). The uncertainty in the central peak location corresponds to an angular resolution for the setup used here of 0.35 nrad misalignment between crystals for two days of measurement. This sensitivity can conceivably be increased by two or more orders of magnitude by using thicker diffracting crystals, blocking the non-interfering portions of the outgoing beam, and running a dedicated experiment for ~1 month, making angular deflection measurements at the prad level a possibility.

B. Intrinsic Bragg-Plane Misalignment

Intrinsic misalignment of Bragg planes has been observed in two-blade interferometers before by Arthur et al. [5]. We are able to measure the intrinsic misalignment between the second and third blade here. The intrinsic misalignments elsewhere in the interferometer are indistinguishable from the relative alignment of the prisms. We form fit functions by substituting

$$
\begin{aligned}
u &\to a\delta_p + u_0 \\
w &\to a\delta_p + w_0
\end{aligned}
\tag{18}
$$

into Eqns. 8 and 9, where a is a fit parameter that has to do with the prism material and neutron wavelength, and δ_p is given by Eqn. 17. If there is an offset in the prism counter rotation, $\phi \to \phi + \phi_0$ in Eqn. 17, then to first order in ϕ_0 this adds the same constant offset to u_0 and w_0. Inserting Eqn. 18 into Eqn. 9, the form of the RRR beam intensity is given by

$$
I \propto \frac{J_2(u_0 - w_0)}{(u_0 - w_0)^2} + \frac{J_2(a\delta_p + u_0)}{(a\delta_p + u_0)^2} + \frac{J_2(a\delta_p + w_0)}{(a\delta_p + w_0)^2}. \tag{19}
$$

The first term only changes the peak baseline, which is absorbed into the A and B fit parameters below. Combing this result with the RR result, we now have two fit functions with related parameters:

$$
I_{RR} = A_1 + B_1 \frac{J_1(a\delta_p + u_0)}{(a\delta_p + u_0)^2} \tag{20}
$$

$$
I_{RRR} = A_2 + B_2 \left[\frac{J_2(a\delta_p + u_0)}{(a\delta_p + u_0)^2} + \frac{J_2(a\delta_p + w_0)}{(a\delta_p + w_0)^2} \right], \tag{21}
$$

where $\{A_{1,2}, B_{1,2}, a, u_0, w_0\}$ are fit parameters, and δ_p is the independent variable given by the prism counter rotation (Eqn. 17). Here we have let the prism counter rotation misalignment be absorbed into u_0 and w_0, such that

$$
\begin{aligned}
u_0 &\to u_c + u_p = u_c + w_p \\
w_0 &\to w_c + w_p = w_c + u_p,
\end{aligned}
\tag{22}
$$

where the c and p subscripts refer to the intrinsic crystallographic misalignment and the effective misalignment from an unknown offset in the prism counter rotation, respectively, and we have noted that $w_p = u_p$. In short, the RR peak is located at u_0 and the RRR peak location is $(u_0 + w_0)/2$. As a result, computing the misalignment $u_0 - w_0 = u_c - w_c$ automatically removes the effective misalignment from the prism counter rotation offset, ϕ_0.

Fitting the RR curve (Fig. 5a) to Eqn. 20 gives $\frac{u_0}{HD} = (16.37 \pm 0.31)$ nrad. Combining this result with the RRR fit of Fig. 5b to Eqn. 21 yields $\frac{w_0}{HD} = (4.75 \pm 0.66)$ nrad, leading to a measured absolute misalignment, $\frac{u_0 - w_0}{HD} = \frac{u_c - w_c}{HD} = (11.57 \pm 0.89)$ nrad for the first interferometer. Both fits have reduced χ^2 (DOF $= 31 - 4$) of 2.8. The uncertainties quoted here do not use expanded error bars to decrease the reduced χ^2 to 1. Doing so increases the quoted uncertainties by a factor of $\sqrt{2.8} \simeq 1.7$.

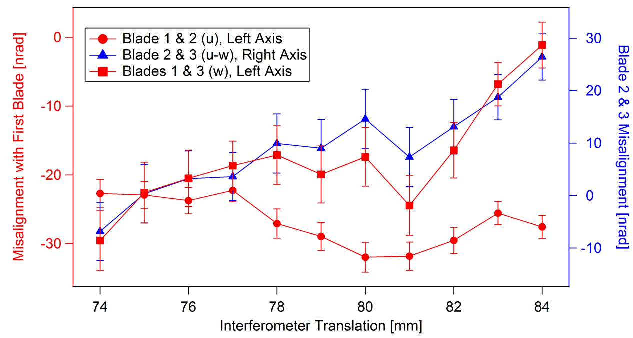

FIG. 7: Misalignments as a function of interferometer translation. The measured misalignments between Blades 1 & 2 and Blades 1 & 3 are shifted depending on a possible offset in the prism counter rotation (red data, left axis), while the misalignment between Blades 2 & 3 is an absolute measurement (blue data, right axis).

When the second interferometer was translated, we found a variation in misalignment on the order of 4 nrad/mm. Shown in Fig. 7 are the measured rocking curve positions as a function of interferometer translation. This suggests that the variation in crystallographic misalignment within each diffracting crystal is large enough to be relevant. If crystallographic misalignments are taken to be fields instead of constants, then the integrals over Γ as well as the solutions to Shrödinger's equation within the crystal are perturbed. These effects, which we do not take into account in our fits of the RR and RRR intensity, as well as the discussion in the next subsection, help explain the poor reduced χ^2 for both the RR and RRR fits.

C. Rocking Curve Fine Structure

If the $P(D)$ terms in Eqn. 3 are not neglected in regards to the RR curve, the fit can be improved. An outline of the fit functions used is given in Appendix C. Keeping the $P(D)$ terms adds three more parameters to the fit

$$
\left\{ \frac{|v_H|(D_2 - D_1)}{k_z}, \frac{|v_H|D}{k_z}, \frac{\sigma_{kz}}{k_z} \right\}. \tag{23}
$$

In this context D is the average of the crystal thicknesses. The reduced χ^2 (DOF $= 31 - 4$) when using Eqn. 20 as a fit function was 2.8. If $|v_H|D/k_z$ is allowed to be a fit parameter, the reduced χ^2 (DOF $= 31 - 5$) falls to 1.9. It was found that $|v_H|(D_2 - D_1)/k_z$ and σ_{kz}/k_z did not impact the quality of the fit. However, a range for each can be computed given what we know about the thicknesses of the interferometer blades and the phase space profile of the incoming neutron beam. For the beam used here, $\sigma_{kz}/k_z \sim 0.0015$ rad, which only attenuates the $P(D)$ terms by a few percent, and the crystal thicknesses are thought to be the same to a few microns.

Even though the parameters $|v_H|(D_2 - D_1)/k_z$ and σ_{kz}/k_z do not improve the fit, they are covariant with u_0 and $|v_H|D/k_z$. As such, assuming a possible range of values for the difference in crystal thicknesses and the beam divergence slightly changes the best fits for the rocking curve peak position and silicon structure factor. We should therefore include a systematic uncertainty when reporting rocking curve peak positions. By performing fits over the acceptable ranges of $|v_H|(D_2 - D_1)/k_z$ and σ_{kz}/k_z, we find a systematic uncertainty in $\frac{u_0}{HD}$ and $|v_H|D/k_z$ of 0.08 nrad and 0.15 nrad, respectively. This leaves us with $x \pm \sigma_{\text{stat}} \pm \sigma_{\text{sys}}$ of $\frac{u_0}{HD} = (-16.49 \pm 0.32 \pm 0.08)$ nrad and $|v_H|D/k_z = (220.29 \pm 0.25 \pm 0.15)$ with $\chi^2_{\text{red}} = 1.9$ for DOF $= 31 - 5$.

The still large reduced χ^2 of 1.9 indicates there may be additional complications to the rocking curve structure. This is likely due to *variation* in crystallographic misalignment between crystal blades demonstrated in Subsec. IV B. Our fit of $|v_H|D/k_z$ corresponds to a sensitivity to v_H of one part in 10^{-3}, which is the level at which the neutron electron scattering length impacts v_H. However, the uncertainty in the Debye-Waller factor prevents a measurement of the neutron electron scattering length from being performed with only one Bragg diffraction [15]. Our sensitivity to v_H is not surprising, as two-crystal rocking curves have been used to measure the X-ray silicon structure factor [25]. In that case the impact of the incoming momentum space profile has also been studied [26]. While the net misalignment between the two diffracting crystals of the RR curve does not affect a measurement of v_H, the same cannot be said for the setups used in [10–12] or [16], where extra diffracting crystals are placed in a Mach-Zhender neutron interferometer. However, all Bragg diffraction measurements of v_H are subject to possible systematics caused by variations in $\boldsymbol{H}$ within the diffracting crystal(s). Our measurement of the spatial dependence of Bragg plane misalignments discussed in Subsec. IV B suggests this effect is not negligible. We leave the analysis of the impact of such stress fields on rocking curves and Pendellösung interference as future work.

V. IMPLICATIONS FOR GRAVITATIONALLY-INDUCED QUANTUM INTERFERENCE EXPERIMENTS

In the COW gravitationally-induced quantum interference experiments, a Mach-Zehnder neutron interferometer is tilted about the incoming beam axis to induce a gravitational phase shift between paths of the interferometer from the earth's gravitational field (Fig. 4b). The resulting phase shift versus $\sin\phi$, where ϕ is the interferometer tilt angle, is predicted to be linear, with the slope, q_{grav}, the measured value to be compared to theory. The primary contribution to q_{grav} is due to the path separation in the earth's gravitational field, but a few corrections are needed.

Dynamical phase effects contributed a perturbation in the expected phase shift for the COW experiments. The Sagnac effect constituted another correction, and bending of the interferometer crystal itself was accounted for using simultaneous neutron, X-ray measurements [8]. Later experiments used two neutron wavelengths to account for the crystal bending [9, 13]. We will focus on data from [8], which used the X-ray technique, because it is more easily analyzed from information given in the article. For a history and more thorough description of the COW experiments see [20].

When the interferometer is tilted in the COW geometry, the beam between crystal blades is deflected by up to about 100 nrad by gravity, leading to the dynamical phase correction. We measured misalignments between diffracting crystals on the order of 10 nrad to 40 nrad. The relative size of the intrinsic misalignments and gravitational deflection imply that the natural misalignment of the interferometer is large enough to perturb the predicted dynamical phase shift. This is a likely explanation for the dynamical phase in the COW experiments being consistently smaller than predicted. Recalculating the dynamical phase contribution to the gravitationally-induced phase shift, while allowing for intrinsic crystal misalignment, we find that including non-zero Bragg-plane misalignments attenuates the dynamical phase contribution (Figs. 8a and 8c) and also impacts the predicted loss of contrast as a function of interferometer tilt (Fig. 8b). Here we have assumed the phase shift due to the bending of the interferometer under its own weight to already be accounted for by the simultaneous X-ray measurement. The distortion of the theoretical contrast and dynamical phase contribution are due to net misalignments that we have not allowed to change upon tilting the interferometer. The nonlinear nature of the dynamical phase and contrast corrections and the three degrees of freedom create the predicted distortions of the dynamical phase and contrast response. The correction from reasonable misalignments as measured in this work is of the correct size to account for the discrepancy between theory and experiment in [8].

There are too many relevant parameters that would need to be measured to recompute the dynamical phase correction for previous COW experiments with intrinsic crystallographic misalignments in the interferometer crystal included. However, for the interferometer used in [8], we were able to find a set of misalignments $\frac{\{u_c, v_c, w_c\}}{HD} = \{\delta_u, \delta_v, \delta_w\} = \{-39.2\,\text{nrad}, -10.7\,\text{nrad}, -3.5\,\text{nrad}\}$ that were consistent with q_{grav} and fitted to normalized contrast, $\frac{C(\phi)}{C(0)}$ (Fig. 8b). A fit to contrast versus tilt angle cannot determine all three misalignment parameters. As a result, the fit to contrast was performed with the theoretical value of q_{grav} fixed to be the value measured in [8]. Additionally, to see that misalignments tend to decrease the theoretical value of q_{grav}, Fig. 8c shows q_{grav} as a function of misalignment with $\delta_u = \delta_v$ and $\delta_w = 0$, compared to the measured value from [8].

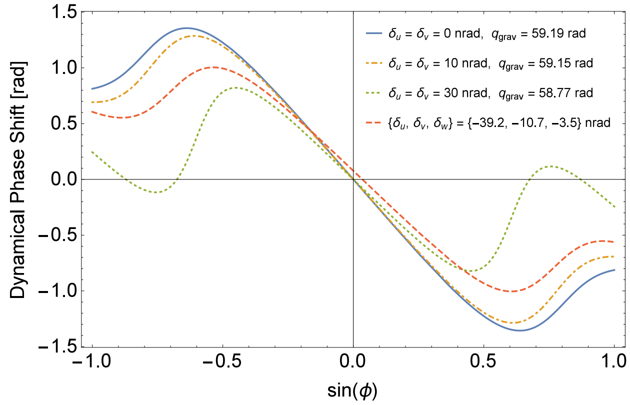

(a) Dynamical phase (Eqn. 14) for the interferometer used in [8] were it to have intrinsic misalignments. The corresponding theoretical values of q_{grav} are given in the legend. The final curve has q_{grav} set to the measured value of (58.72 ± 0.03) rad [8].

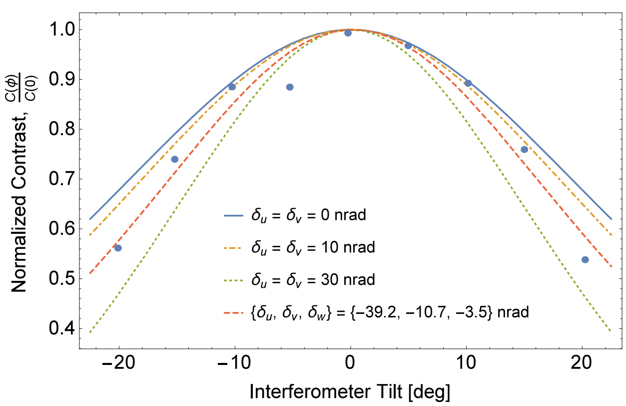

(b) Normalized contrast (Eqn. 15) vs. tilt for the interferometer used in [8] were it to have intrinsic misalignments. Data points are from [8]. Uncertainties were not reported.

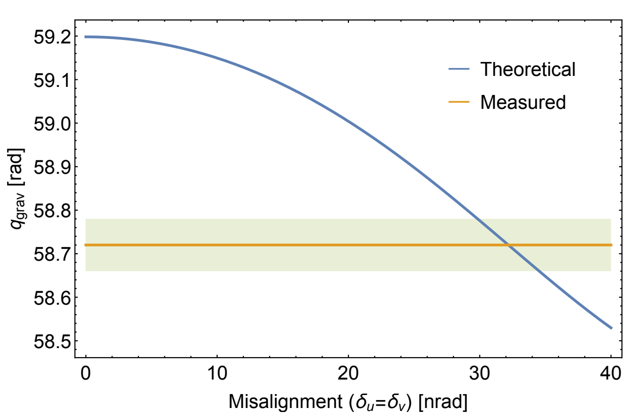

(c) Theoretical slope of the gravitational phase shift as a function of $\delta_u = \delta_v$ crystal misalignment with $\delta_w = 0$. Experimental results $\pm 2\sigma$ from [8] are also shown.

FIG. 8

The predicted contrast at no tilt with $\{\delta_u, \delta_v, \delta_w\} = \{-39.2\,\text{nrad}, -10.7\,\text{nrad}, -3.5\,\text{nrad}\}$ for the interferometer used in [8] is 81 %, to be compared with the measured value of 59 %. Fits to absolute contrast, instead of normalized contrast, yielded poor results, suggesting that there are other factors contributing to loss of contrast in this interferometer. The variation in misalignments within diffracting crystals as discussed in Subsec. IV B or environmental factors such as vibrations are possible culprits.

A two crystal interferometer such as the one used in [5] may be able to resolve the disagreement between theory and experiment for gravitationally-induced quantum interference using silicon neutron interferometers. If such an interferometer were tilted along the beam axis, deflection due to gravity would shift the central interference peak. As we have shown here, complications from crystal blade misalignments can be measured for such an interferometer in a fairly direct manner. Only the centroid of the rocking curve would be affected due to gravity and the Sagnac effect, the consequences of which are calculable.

Finally, we note that gravitationally-induced quantum interference has since been found to agree with theory at the 0.1% level using a spin-echo neutron interferometer [27] and at 0.08% with a very cold grating neutron interferometer [28]. Atom interferometer experiments have confirmed theory at the part per billion level [20].

The effect of intrinsic misalignments in neutron interferometers does not end with gravitationally-induced quantum interference. In the experiment performed in [10], a measurement of the dynamical phase upon Laue transmission resulted in a weaker dynamical phase response than predicted. It is unclear whether including nonzero intrinsic interferometer misalignments would explain the discrepancy.

VI. CONCLUSION

Measurements that rely on dynamical phases in neutron interferometry require careful characterization of imperfections in the interferometer crystal. Crystal misalignments on the 10 nrad to 40 nrad level, as well as a dependence on Pendellösung oscillations have been measured for two monolithic silicon neutron interferometers at the NCNR. Such crystallographic imperfections may affect future precision measurements of the silicon structure factor and provide a likely explanation for the discrepancy between theory and experiment in the COW gravitationally-induced quantum interference measurements. Rocking curve interference peaks have the potential to measure very small deflections (on the order of prad) of the neutron beam in an interferometer, as well as characterize the strain in Mach-Zehnder neutron interferometers.

ACKNOWLEDGMENTS

The authors would like to acknowledge Samuel Werner for leading the long effort to precisely measure gravitationally-induced quantum interference with neutron interferometers. We would also like to thank Michael Snow and Fred Wietfeldt for fruitful discussions. This work was supported in part by the US Department of Energy under Grant No. DE-FG02-97ER41042, National Science Foundation Grant No. PHY-1307426 and Grant No. PHY-1205342, Canadian Excellence Research Chairs (CERC) (215284), Natural Sciences and Engineering Research Council of Canada (NSERC) Discovery (RGPIN-418579), Collaborative Research and Training Experience (CREATE) (414061), and the NIST Quantum Information Program.

Appendix A: Energy eigenstates of the Dynamical Diffraction Hamiltonian

We wish to find solutions to the dynamical diffraction Hamiltonian [18]:

$$H = \frac{\hbar^2}{2m}k^2 + \frac{2\pi\hbar^2}{m}\sum_{\ell,v} b_{\ell,v}\delta(\boldsymbol{r}-\boldsymbol{r}_{\ell,v}), \tag{A1}$$

where $b_{\ell,v}$ is the scattering length of the nucleus located at $\boldsymbol{r}_{\ell,v}$; ℓ indexes the unit cells; and v indexes position within the crystal cell. It is customary to expand Eqn. A1 in momentum space:

$$\frac{2m}{\hbar^2}H = (K^2+v_0)|\boldsymbol{K}\rangle\langle\boldsymbol{K}| + (K_H^2+v_0)|\boldsymbol{K}_H\rangle\langle\boldsymbol{K}_H| + \\ + v_H|\boldsymbol{K}\rangle\langle\boldsymbol{K}_H| + v_{-H}|\boldsymbol{K}_H\rangle\langle\boldsymbol{K}|, \tag{A2}$$

where $\boldsymbol{K}_H \equiv \boldsymbol{K}+\boldsymbol{H}$, and v_q is the neutron-silicon structure factor per unit cell, given by [18]:

$$v_q = e^{-W}\frac{4\pi}{\Omega_0}\sum_v b_v e^{i\boldsymbol{r}_v\cdot\boldsymbol{q}}, \tag{A3}$$

where e^{-W} is the Debye-Waller factor and Ω_0 is the volume of a unit cell. This Hamiltonian leads to the secular equation

$$(K^2+v_0-k^2)(K_H^2+v_0-k^2) = |v_H|^2, \tag{A4}$$

where we have suggestively labeled our energy eigenvalue (with $\hbar^2/2m$ factored out) as k^2. This will later turn out to be the momentum of an incoming momentum mode, $|\boldsymbol{k}_0\rangle$. Solving the secular equation for a fixed momentum, $\boldsymbol{K}$, gives

$$k^2 = K^2 + v_0 + \frac{1}{2}(K_H^2 - K^2) + \\ \pm\sqrt{\frac{1}{4}(K^2-K_H^2) + |v_H|^2}. \tag{A5}$$

The energy states of the dynamical diffraction Hamiltonian therefore make up a continuous spectra with a two-fold degeneracy formed by two momentum states, which we now call $\boldsymbol{K}^{\pm}$

$$K^{\pm^2} = k^2 - v_0 + v_H\left(-\eta \pm \sqrt{\eta^2+1}\right), \tag{A6}$$

where

$$\eta \equiv \frac{K_H^2 - K^2}{2|v_H|} = \frac{\boldsymbol{\delta K}\cdot\boldsymbol{H}}{|v_H|} \tag{A7}$$

with $\boldsymbol{\delta K}$ being the deviation from the exact Bragg condition. The corresponding value of $K_H^{\pm^2}$ is then

$$K_H^{\pm^2} = k^2 - v_0 + v_H\left(\eta \pm \sqrt{\eta^2+1}\right). \tag{A8}$$

We are now ready to write down the energy eigenstates of the dynamical diffraction Hamiltonian

$$|\boldsymbol{K},\pm\rangle = a_0^{\pm}(K)\,|\boldsymbol{K}\rangle + a_H^{\pm}(K)\,|\boldsymbol{K}_H\rangle \tag{A9}$$

with the coefficients

$$a_0^{\pm}(K) = \frac{1}{\sqrt{2}}\left(1 \pm \frac{K_H^2-K^2}{2\sqrt{\frac{1}{4}\left(K_H^2-K^2\right)^2+|v_H|^2}}\right)^{\frac{1}{2}}$$

$$a_H^{\pm}(K) = \mp\frac{1}{\sqrt{2}}\left(\mp 1 + \frac{K_H^2-K^2}{\sqrt{\frac{1}{4}\left(K_H^2-K^2\right)^2+|v_H|^2}}\right)^{\frac{1}{2}},$$

or in terms of the customary $\eta = \boldsymbol{k}\cdot\boldsymbol{H}/|v_H|$ parameter (which will replace $\boldsymbol{K}$ in the $\boldsymbol{H}$ direction as an integration variable)

$$a_0^{\pm}(\eta) = \frac{1}{\sqrt{2}}\left(1 \pm \frac{\eta}{\sqrt{\eta^2+1}}\right)^{\frac{1}{2}} \tag{A10}$$

$$a_H^{\pm}(\eta) = \mp\frac{1}{\sqrt{2}}\left(1 \mp \frac{\eta}{\sqrt{\eta^2+1}}\right)^{\frac{1}{2}}. \tag{A11}$$

Additionally, it can be shown that the $\pm$ states traverse a distance $x'-x$ along the crystal

$$x'-x=\mp\mathrm{sign}(H_x)\frac{\eta}{\sqrt{\eta^2+1}}D\tan\theta_B. \tag{A12}$$

It is usually more useful to switch from the $\{\pm\}$ basis to the $\{\alpha,\beta\}$ basis where $\mathrm{sign}(J_x^{\alpha,\beta})=\pm\mathrm{sign}(H_x)$, which simply requires that [20]

$$\pm\rightarrow-\mathrm{sign}(\eta)\quad(\alpha\text{ branch})$$

$$\pm\rightarrow\mathrm{sign}(\eta)\quad(\beta\text{ branch})$$

for the $\pm$ in the equations above.

Appendix B: Mach-Zehnder Geometry Calculations

Following previous work [2, 8, 9, 23], but generalizing to let there be three separate misalignments $\{u,v,w\}$, gives

$$\begin{aligned}\langle\mathrm{I}|\mathrm{I}\rangle=\pi\Bigg[&8\frac{J_1(v-w)}{u-w}-12\frac{J_2(v-w)}{(v-w)^2}+\\&-12\frac{J_2(v)}{v^2}-12\frac{J_2(w)}{w^2}+5\Bigg]\end{aligned} \tag{B1}$$

$$\begin{aligned}\langle\mathrm{II}|\mathrm{II}\rangle=\pi\Bigg[&8\frac{J_1(u)}{u}-12\frac{J_2(u-w)}{(u-w)^2}+\\&-12\frac{J_2(u)}{u^2}-12\frac{J_2(w)}{w^2}+5\Bigg]\end{aligned} \tag{B2}$$

$$\begin{aligned}\mathrm{Im}\left[\langle\mathrm{I}|\mathrm{II}\rangle\right]=4\pi\Bigg[&\frac{J_2\left(\frac{u+v}{2}\right)}{\frac{u+v}{2}}-\frac{J_2\left(\frac{u-v}{2}-w\right)}{\frac{u-v}{2}-w}+\\&+\frac{J_2\left(\frac{u-v}{2}+w\right)}{\frac{u-v}{2}+w}-\frac{J_2\left(\frac{u+v}{2}-w\right)}{\frac{u+v}{2}-w}\Bigg]\end{aligned} \tag{B3}$$

$$\begin{aligned}\mathrm{Re}\left[\langle\mathrm{I}|\mathrm{II}\rangle\right]=2\pi\Bigg[&4\frac{J_1\left(\frac{u-v}{2}\right)}{\frac{u-v}{2}}-12\frac{J_2\left(\frac{u-v}{2}\right)}{\left(\frac{u-v}{2}\right)^2}+\\&+2\frac{J_1\left(\frac{u+v}{2}\right)}{\frac{u+v}{2}}-6\frac{J_2\left(\frac{u+v}{2}\right)}{\left(\frac{u+v}{2}\right)^2}+\\&+2\frac{J_1\left(\frac{u-v}{2}-w\right)}{\frac{u-v}{2}-w}-3\frac{J_2\left(\frac{u-v}{2}-w\right)}{\left(\frac{u-v}{2}-w\right)^2}+\\&+2\frac{J_1\left(\frac{u+v}{2}-w\right)}{\frac{u+v}{2}-w}-6\frac{J_2\left(\frac{u+v}{2}-w\right)}{\left(\frac{u+v}{2}-w\right)^2}+\\&+2\frac{J_1\left(\frac{u-v}{2}+w\right)}{\frac{u-v}{2}+w}-3\frac{J_2\left(\frac{u-v}{2}+w\right)}{\left(\frac{u-v}{2}+w\right)^2}\Bigg]\end{aligned} \tag{B4}$$

for the 0 Beam. The phase and contrast of a regular interferogram can then be extracted by inserting these expressions into Equations 14 and 15.

Appendix C: Rocking Curve Fine Structure

We wish to estimate Eqn. 3 in terms of a set of parameters, $\left\{HD\delta,\frac{D|v_H|}{k_z},\frac{\sigma_{kz}}{k_z},\frac{(D_2-D_1)|v_H|}{k_z}\right\}=\{\mu,\Delta,\sigma,\xi\}$, which corresponds to integrals of the form

$$\mathcal{I}=\int d\Gamma\,\sqrt{1-\Gamma^2}\cos\left(\mu\Gamma\right)\cos\left(\frac{\Delta}{\sqrt{1-\Gamma^2}}\right). \tag{C1}$$

Because the blades of the interferometer are nearly the same thickness, the $P(D_2-D_1)$ term in Eqn. 3 can be expanded in terms of $\Delta\rightarrow\xi$

$$\begin{aligned}\mathcal{I}&=\int d\Gamma\,\sqrt{1-\Gamma^2}\cos(\mu\Gamma)\left(1-\frac{\xi^2}{2(1-\Gamma^2)}+\mathcal{O}(\xi^4)\right)\\&=\pi\left(\frac{J_1(\mu)}{\mu}-\frac{\xi^2}{2}J_0(\mu)+\mathcal{O}(\xi^4)\right).\end{aligned} \tag{C2}$$

This approximation is found to have an error of less than 0.5% of the peak maximum for $\xi=0.2$ and any value of μ. The $P(D)$ terms in Eqn. 3, on the other hand, are extremely oscillatory, so we integrate over $\langle\psi|k_z\rangle\langle k_z|\psi\rangle$ and use a stationary phase method, similar to [29, 30]. In this case, is better to integrate over η than Γ:

$$\begin{aligned}\mathcal{I}=\mathrm{Re}\Bigg\{\int d\eta\,\exp\Bigg[&i\mu\frac{\eta}{\eta^2+1}+i\Delta\sqrt{\eta^2+1}+\\&-\frac{1}{2}(\eta^2+1)\Delta^2\sigma^2-2\log\left(\eta^2+1\right)\Bigg]\Bigg\}.\end{aligned} \tag{C3}$$

We then expand the argument of the exponential, $f(\eta)$, around η_0 which should be close to a minimum of $f(\eta)$.

To avoid having to numerically find η_0, we neglect terms η_0^2 and higher in $f^{(1)}(\eta_0) = 0$, which gives

$$\eta_0 = \frac{i\mu}{\Delta^2\sigma^2 - i\Delta + 4}. \tag{C4}$$

We then neglect terms in the argument of the exponential of $(\eta - \eta_0)^3$ and higher and complete the integral as a Gaussian

$$\mathcal{I} = \mathrm{Re}\left\{\sqrt{2\pi}\frac{\exp\left[f(\eta_0) - \frac{f^{(1)}(\eta_0)^2}{2f^{(2)}(\eta_0)}\right]}{\sqrt{-f^{(2)}(\eta_0)}}\right\}. \tag{C5}$$

This function is found to have an error of less that 0.5% of the peak value over the relevant ranges of $\{\mu, \Delta, \sigma\}$.

[1] C. Shull, Physical Review Letters **21**, 1585 (1968).

[2] U. Bonse, W. Graeff, R. Teworte, and H. Rauch, physica status solidi (a) **43**, 487 (1977).

[3] U. Bonse, W. Graeff, and H. Rauch, Physics Letters A **69**, 420 (1979).

[4] H. Rauch, U. Kischko, D. Petrascheck, and U. Bonse, Zeitschrift für Physik B Condensed Matter **51**, 11 (1983).

[5] J. Arthur, C. G. Shull, and A. Zeilinger, Physical Review B **32**, 5753 (1985).

[6] U. Bonse and T. Wroblewski, Physical Review D **30**, 1214 (1984).

[7] M. A. Horne, Physica B+ C **137**, 260 (1986).

[8] S. A. Werner, H. Kaiser, M. Arif, and R. Clothier, Physica B+ C **151**, 22 (1988).

[9] K. C. Littrell, B. E. Allman, O. Motrunich, and S. A. Werner, Acta Crystallographica Section A: Foundations of Crystallography **54**, 563 (1998).

[10] J. Springer, M. Zawisky, H. Lemmel, and M. Suda, Acta Crystallographica Section A: Foundations of Crystallography **66**, 17 (2009).

[11] M. Zawisky, J. Springer, R. Farthofer, and U. Kuetgens, Nuclear Instruments and Methods in Physics Research Section A: Accelerators, Spectrometers, Detectors and Associated Equipment **612**, 338 (2010).

[12] T. Potocar, M. Zawisky, H. Lemmel, J. Springer, and M. Suda, Acta Crystallographica Section A: Foundations and Advances **71**, 534 (2015).

[13] K. C. Littrell, B. E. Allman, and S. A. Werner, Physical Review A **56**, 1767 (1997).

[14] R. Colella, A. W. Overhauser, and S. A. Werner, Physical Review Letters **34**, 1472 (1975).

[15] J.-M. Sparenberg and H. Leeb, Journal of electron spectroscopy and related phenomena **129**, 315 (2003).

[16] F. Wietfeldt, M. Huber, T. C. Black, H. Kaiser, M. Arif, D. Jacobson, and S. Werner, Physica B: Condensed Matter **385**, 1374 (2006).

[17] G. L. Greene and V. Gudkov, Physical Review C **75**, 015501 (2007).

[18] V. F. Sears, Canadian Journal of Physics **56**, 1261 (1978).

[19] H. Lemmel, Acta Crystallographica Section A: Foundations of Crystallography **69**, 459 (2013).

[20] H. Rauch and S. A. Werner, *Neutron Interferometry: Lessons in Experimental Quantum Mechanics, Wave-particle Duality, and Entanglement*, 2nd ed. (Oxford University Press, 2015).

[21] C. G. Shull and J. Oberteuffer, Physical Review Letters **29**, 871 (1972).

[22] C. Shull and W. Shaw, Zeitschrift für Naturforschung A **28**, 657 (1973).

[23] D. Petrascheck and H. Rauch, Acta Crystallographica Section A: Foundations of Crystallography **40**, 445 (1984).

[24] D. Pushin, D. Cory, M. Arif, D. Jacobson, and M. Huber, Applied physics letters **90**, 224104 (2007).

[25] R. Teworte and U. Bonse, Physical Review B **29**, 2102 (1984).

[26] U. Bonse and R. Teworte, Zeitschrift für Naturforschung A **37**, 427 (1982).

[27] V. O. de Haan, J. Plomp, A. A. van Well, M. T. Rekveldt, Y. H. Hasegawa, R. M. Dalgliesh, and N.-J. Steinke, Physical Review A **89**, 063611 (2014).

[28] G. Van der Zouw, M. Weber, J. Felber, R. Gähler, P. Geltenbort, and A. Zeilinger, Nuclear Instruments and Methods in Physics Research Section A: Accelerators, Spectrometers, Detectors and Associated Equipment **440**, 568 (2000).

[29] N. Kato, Acta Crystallographica **14**, 526 (1961).

[30] N. Kato, Acta Crystallographica **14**, 627 (1961).